Ductile Braze Repairs for Ni-Based Superalloys Using Novel MPEA Filler Metal

A novel multiprincipal-element alloy filler metal provides comparable strength to and enhanced ductility over conventional fillers for superalloy repair

BY B. SCHNEIDERMAN, O. DeNONNO, J. KLEMM-TOOLE, AND Z. YU

Abstract

The performance of a newly developed multiprincipal-element alloy (MPEA) filler metal for brazing of nickel-based superalloys was directly compared to a conventional boron- and silicon-suppressed filler (BSSF) metal. The comparison was demonstrated on an Alloy 600 substrate with a brazing temperature of 1200°C. Single-phase solidification behavior and the absence of boron and silicon in the MPEA led to a joint microstructure devoid of eutectic constituents or brittle phases in brazes employing this filler metal. In the brazes using the conventional BSSF metal, incomplete isothermal solidification and subsequent athermal solidification of the residual liquid resulted in large particles of a chromium-rich boride phase distributed throughout the microstructure. Tensile testing of brazed butt joints at both room temperature and 600°C testing conditions demonstrated that the MPEA joints exhibited total ductility values at least one order of magnitude greater than that of BSSF joints, but they showed comparable yield strengths in both testing conditions. Fractographic assessment confirmed that boride phases nucleated cracks and resulted in brittle failure in the BSSF joints, while the MPEA joints exhibited extensive ductile microvoid coalescence. Fine-scale porosity and oxide inclusions may be the dominant factors limiting the overall ductility observed in the MPEA brazes.

Keywords

- Multiprincipal Element Alloy (MPEA)
- High-Entropy Alloy
- Nickel-Based Superalloy
- Ductile Braze Repair
- High-Temperature Deformation

Introduction

Nickel (Ni)-based superalloys are widely employed in elevated-temperature applications in the power generation and aerospace industries due to their desirable mechanical properties at high temperatures. Despite their exceptional properties, damage mechanisms such as fatigue, creep, and surface degradation cause cracking in Ni-based components during service (Ref. 1). Braze repair processes have been developed over the past several decades in the attempt to prolong component service life. Conventional brazing, in which a molten filler material is briefly flowed into the damage-induced gap or crack, typically employs Ni-based filler materials with boron (B) and/or silicon (Si) added as melting-point depressants (MPDs). Solidification upon cooling leaves behind significant volume fractions of boride or silicide phases within eutectic constituents, which are brittle and degrade joint ductility (Refs. 1, 2).

Transient liquid phase (TLP) brazing, using either a braze filler metal only (Refs. 3–8) or a mixture of filler metal and substrate powder (also called wide-gap brazing or transient liquid phase infiltration [TLI]) (Refs. 1, 9–12), can theoretically eliminate borides and silicides from the microstructure. These processes rely on the rapid diffusion of MPD elements into the substrate material, as shown from stages i to ii in Fig. 1A, causing a local composition change that drives isothermal solidification at a holding temperature. In the case of TLI, substrate powder particles serve as additional diffusion sinks to enable isothermal solidification to
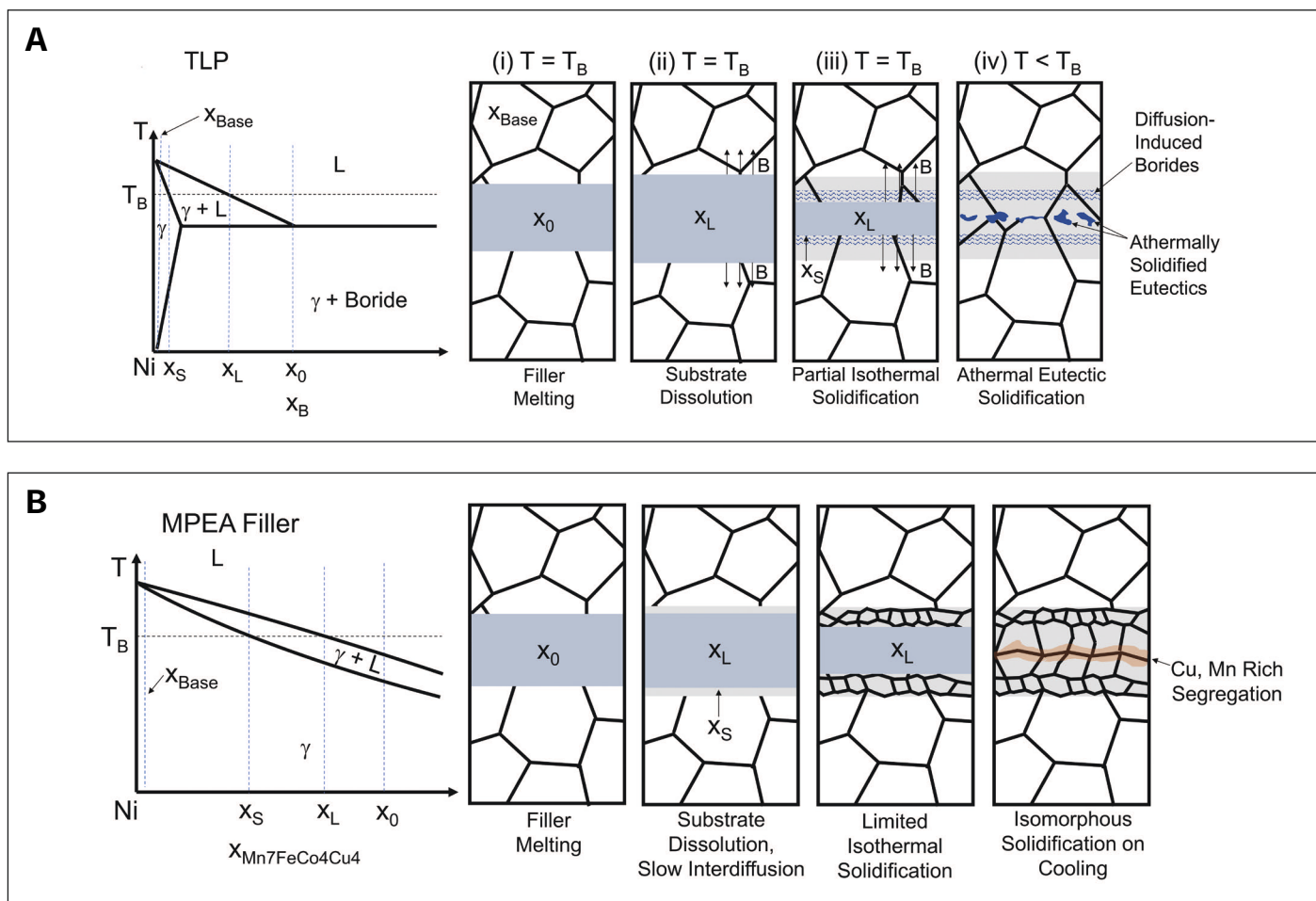
Fig. 1 — Schematic illustrations of the phase diagram and microstructure evolution during brazing using the following: A — Conventional TLP braze filler with formation of secondary phases in the eutectic constituents (modeled after Ref. 6); B — the new MPEA filler metal.

occur with wider joint clearances by shortening necessary diffusion distances (Refs. 1, 9–12). Ideally, TLP and TLI are expected to result in a homogeneous microstructure with no second phases and high-strength brazes with appreciable ductility (Refs. 1, 9). However, homogeneous microstructures are rarely achieved in industrial braze repairs. Full isothermal solidification requires long hold times for MPD diffusion to reduce the solute content to the solidus composition ($\leq x_s$ in the phase diagram shown in Fig. 1A), often on the order of hours for a narrow joint clearance of approximately 25 μm (Refs. 1, 3). Incomplete isothermal solidification may occur if the hold time is insufficient, leaving behind residual liquid that subsequently solidifies athermally as a eutectic mixture during cooling (Refs. 1, 4, 7, 8), as illustrated by stages iii and iv in Fig. 1A.

Furthermore, if the brazing temperature is below the binary eutectic temperature of a pair of elements in the system, diffusion-induced saturation of B or Si beyond the solubility limit (Refs. 4–8) may occur, causing precipitation of borides or silicides in the solid state, as illustrated by stages iii and iv in Fig. 1A. These second phases usually do not redissolve without an additional elevated-temperature heat treatment (Refs. 3, 6). The

role of diffusion-induced boride or silicide phases in the brazed microstructure is important to consider. Literature reports do not isolate the impact of the diffusion-induced boride or silicide precipitates upon mechanical properties; instead, they usually discuss athermally solidified borides and silicides as the primary ductility inhibitors. However, it is noteworthy that poor ductility is often demonstrated even at long process durations. For example, a comprehensive review of mechanical properties in wide joint clearance Ni-based superalloy brazes performed by TLI indicated that the highest room-temperature elongation achieved was 2.3% in a process employing a hold duration of up to 20 h (Ref. 1).

Boron- and Si-free braze filler metals can be employed using conventional brazing cycles of shorter duration, but these are usually based in expensive noble metals, such as Au or Ag (Refs. 13, 14). Miglietti and Du Toit reported studies on Ni-based fillers for conventional brazing in which the MPD elements were replaced by either Hf or Zr (Refs. 15, 16). Most of the resulting microstructures contained eutectic constituents with phases rich in these new MPDs (Refs. 15, 16). Although these eutectics were not as detrimental to ductility as borides or silicides and the joints exhibited a strength approximately 65% of that of the base
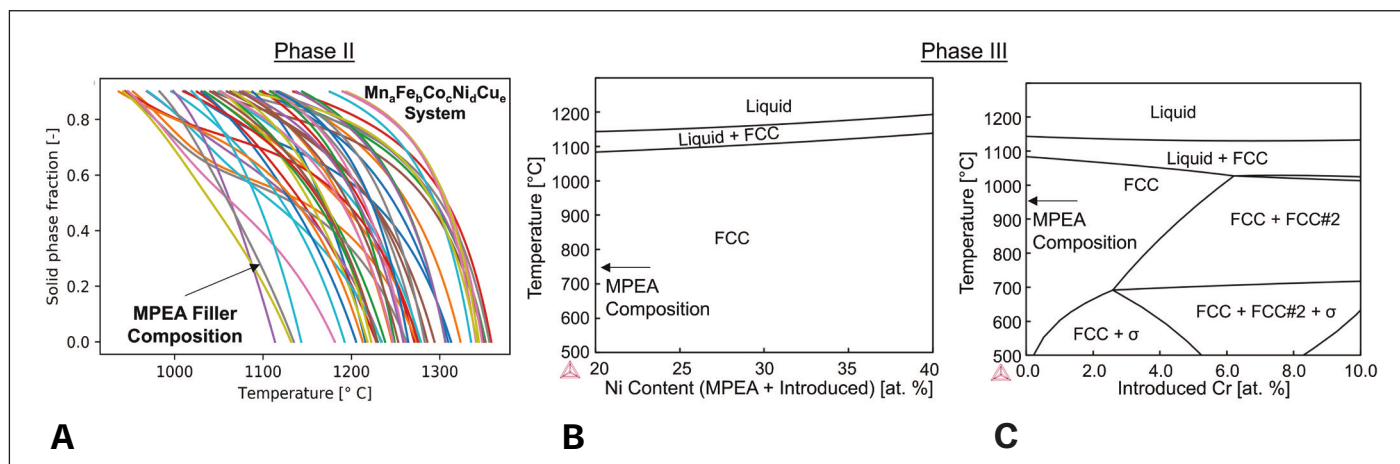
Fig. 2 — A — A subset of the solidification curves output from high-throughput Scheil solidification simulations for the MnFeCoNiCu system in Phase II of the down-selection process; B, C — isopleth phase diagrams in Phase III demonstrating the tolerance of the single-phase behavior of $Mn_{35}Fe_5Co_{20}Ni_{20}Cu_{20}$ to Ni (B) and Cr (C) diffused from the substrate.

material over a range of testing temperatures, the total tensile elongation did not exceed 5% (Refs. 15, 16). Hence, there is a need for superalloy braze repair filler metals that offer a combination of high ductility and strength, short processing durations, and inexpensive constituent elements.

Filler Metal Design Strategy

The authors' research group recently developed a new multi-principal-element alloy (MPEA) filler metal of the approximate composition $Mn_{35}Fe_5Co_{20}Ni_{20}Cu_{20}$ (Refs. 17, 18) to address this challenge. Early theory pertaining to MPEAs predicted several properties that render them attractive candidates for a novel class of filler alloys, including vast design space, single-phase stability (Refs. 19–21), severe lattice distortion (Ref. 22) within a random solid-solution structure, and the potential for sluggish diffusion

(Refs. 23, 24). Lattice distortion may lend itself to desirable high strain-hardening rates and corresponding toughness. Sluggish diffusion may delay undesirable interactions with superalloy substrates during service at elevated temperatures, inhibiting detrimental secondary phases by limiting interdiffusion across the joint interface. Nonetheless, a flexible design space to tune the solidification range and a stable single phase with appreciable ductility are the most important characteristics of MPEAs, giving them the potential to avoid formation of brittle second phases that plague superalloy repair with conventional filler metals. This scenario is illustrated in Fig. 1B, which shows very limited isothermal solidification occurs during the braze holding step, and no second phases precipitate during subsequent solidification of the remaining liquid during cooling.

While more recent studies have questioned the universality of the entropy-stabilized single-phase behavior among MPEAs (Ref.

Table 1 — Nominal Composition (wt-%) of the BSSF Filler Metal (Ref. 33), MPEA Filler Metal, and Alloy 600 Base Material (Ref. 32)

	Ni	Cr	Fe	B	Si	C	Mn	S	Cu	Co
BSSF filler metal	Bal.	7.0	3.0	3.1	4.5	—	—	—	—	—
MPEA filler metal	20.2	—	4.8	—	—	—	33.0	—	21.8	20.2
Alloy 600 base material	72.0 min.	14 0–17.0	6.0–10.0	—	0.50 max.	0.15 max.	1.00 max.	0.50 max.	0.50 max.	—

*Note: The MPEA nominal composition has been converted to wt-% for comparison with the other alloys.
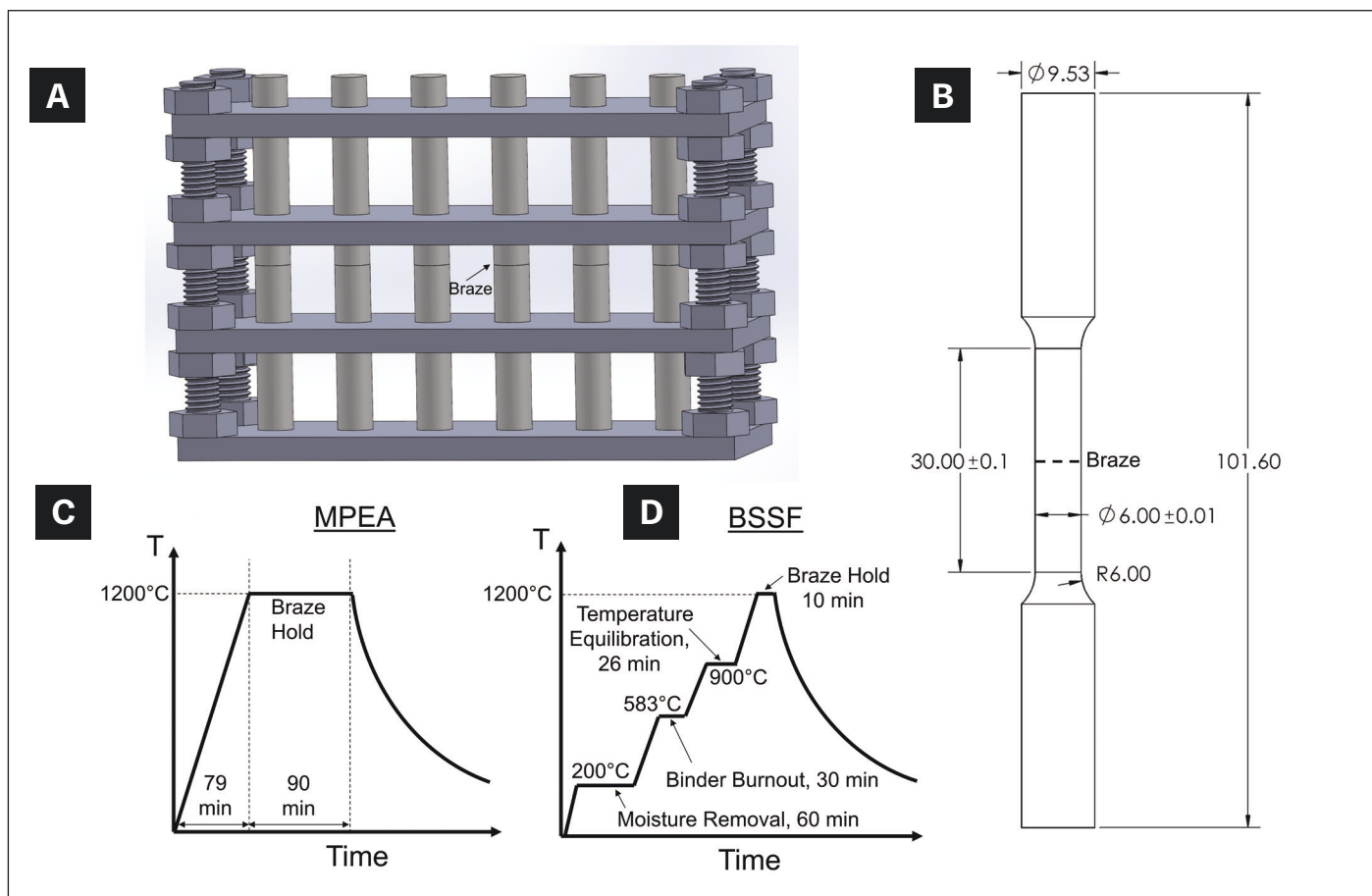
Fig. 3 — A — Schematic illustration of the fixturing assembly employed during brazing; B — drawing of the ASTM E8M specimen machined from each butt joint, where the dimensions are in mm; C, D — thermal profiles employed for brazing with the MPEA filler (C) (Ref. 17) and BSSF filler metal (D) (Ref. 34).

25), there is a general acknowledgment that ductile face-centered cubic (FCC) crystal structures are prevalent among 3d-transition metal MPEAs (Ref. 26). Exploiting this, the specific filler metal composition was down-selected from a set of nine 3d-transition metal elements via a multistep computational approach to filter a large candidate pool. The design criteria governing candidate down-selection were to generate a single-phase FCC microstructure and a sufficiently low liquidus temperature to braze at least 100°C below the solidus temperature of the Alloy 600 substrate (Ref. 17). The down-selection process was subdivided into three phases as described below.

Phase I targeted the selection of an appropriate alloy system or a group of five elements with a high likelihood of exhibiting a single-phase FCC crystal structure over a wide composition space. In MPEA literature, the traditional Hume-Rothery rules (Refs. 27–29) were extended (Refs. 26, 30, 31) to define appropriate ranges for atomic size mismatch, average valence electron concentration, ΔS_{mix} (entropy of mixing), and ΔH_{mix} (enthalpy of mixing) that would favor the stability of disordered solid-solution FCC phases. Of the five-element systems considered, the MnFeCoNiCu system displayed the largest fraction of compositions that lie within the specified ranges for all criteria.

Phase II of the selection process aimed to probe the composition space within an alloy system to seek compositions with an appropriate melting range. This was accomplished by high-throughput Scheil solidification simulations in the Thermo-Calc software performed through the TC-Python™ interface. Figure 2A shows a subset of the solidification curves output from the simulation set on the MnFeCoNiCu system, indicating the variability of the solidification temperature range for compositions within the system. Based on this analysis, $Mn_{35}Fe_5Co_{20}Ni_{20}Cu_{20}$, with the Scheil curve identified in Fig. 2A, was identified as a specific candidate composition. Subsequent equilibrium thermodynamic calculations were employed to estimate the solidification temperature range for this composition under slow furnace-cooled conditions. These calculations predicted a liquidus temperature of 1150°C and a solidus temperature of 1090°C, which were confirmed to match experimental differential thermal analysis results to within 10°C (Ref. 17). This solidification range renders the composition appropriate for brazing at 1200°C, which is approximately 150°C below the solidus temperature of Alloy 600 (Ref. 32). Note that predictions of phases that form upon solidification were also employed in Phase II to corroborate the Phase I filtration outputs.

Finally, Phase III examined whether selected compositions are robust in their single-phase stability after interactions with the
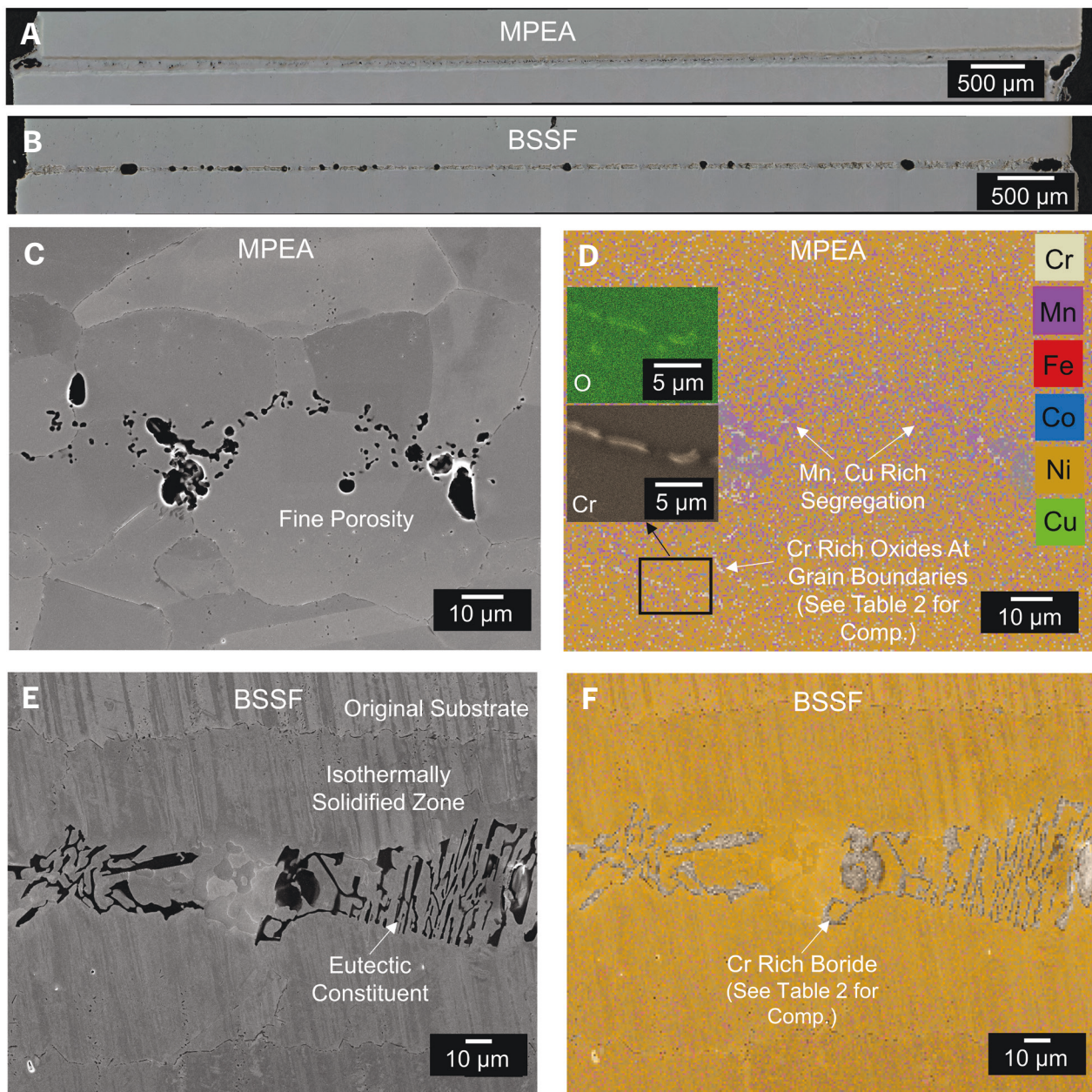
Fig. 4 — Optical micrographs of the braze cross section of the MPEA joint (A) and BSSF joint (B) along with SEM micrographs and EDS element maps of representative braze cross sections of the MPEA (C–D) and BSSF joints (E–F).

superalloy substrate during brazing. As indicated by the isopleth phase diagrams in Fig. 2B and C, $Mn_{35}Fe_5Co_{20}Ni_{20}Cu_{20}$ possesses a high tolerance to dilution in Ni and appreciable tolerance to dilution in Cr without forming second phases. Although as-solidified MPEA microstructures do not represent an equilibrium thermodynamic condition (Ref. 18), the calculated phase diagrams can nonetheless offer insight regarding the robustness of single-phase stability. The initial feasibility study confirmed that this overall strategy was successful in selecting a viable filler metal composition (Ref. 17). For the $Mn_{35}Fe_5Co_{20}Ni_{20}Cu_{20}$ MPEA, the phase diagram is isomorphous with a narrow solid-

ification range, and all the constituent MPEA elements diffuse into the substrate at similar rates (Ref. 17), which prevents local supersaturation of a particular element. Neither postmortem microstructural characterizations nor in-situ examination of the MPEA solidification behavior (Ref. 18) showed intermetallic phases under the optimum brazing conditions (Ref. 17). For joints brazed using optimized parameters, room temperature shear strengths of up to 530 MPa were reported for brazed lap joints in the original study (Ref. 17). However, cracked Ni-based superalloy components that are repaired and returned to service are more likely to exert tensile stresses on the filler metal and operate at
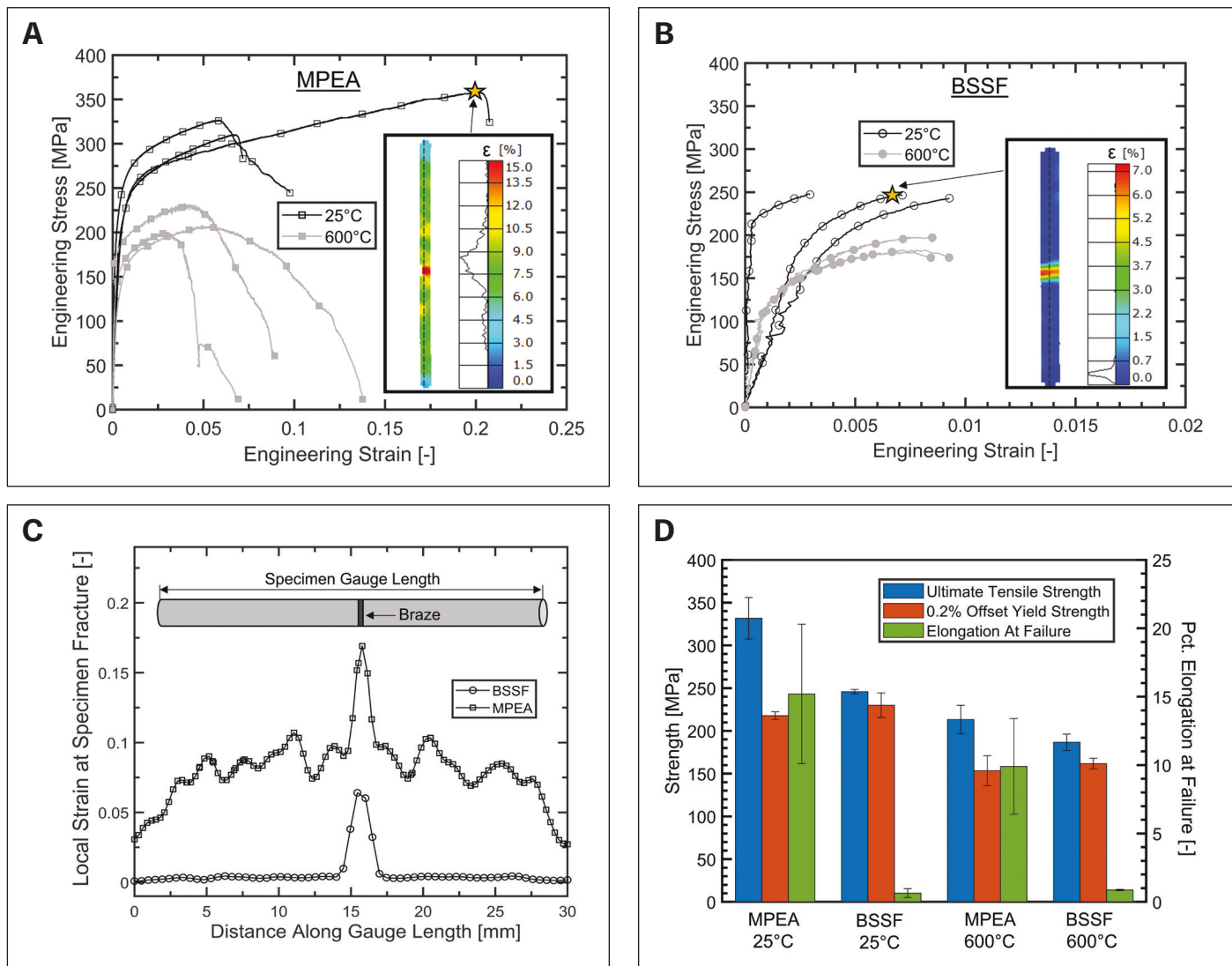
Fig. 5 — A, B — Engineering stress-strain data for room-temperature and 600°C tests for joints brazed using the MPEA filler metal (A) and BSSF filler metal (B). Note the difference in the x-axis scaling. The insets show strain-partitioning maps generated from digital image correlation, which was taken at the loading conditions indicated on the stress-strain curves. The adjoining plots in the insets qualitatively show the fractional distribution of the assessed area that experiences particular strain values; C — comparison of cross-sectional strain profiles at the locations indicated by the dashed lines in the insets in A and B; D — summary of mechanical properties, with error bars representing one standard deviation.

elevated temperatures. The objective of this study was to identify both room- and high-temperature tensile properties of the MPEA braze and compare them directly to those of a conventional braze.

Experimental Methods

As illustrated in Fig. 3A, cylindrical rods of Ni-based Alloy 600 ⅜ in. in diameter and 2 in. long were stacked vertically end to end and brazed to form a butt joint. Stainless steel fixturing was engineered to ensure good alignment, and a Continental Braze Supply LLC Pro-Stop Braze 700V was employed to prevent bonding to the fixture. Specimens were brazed using one of two types of filler metals: a 300-μm-thick MPEA filler metal foil manufactured as detailed in Gao et al. (Ref. 17) or a commercially available B- and Si-suppressed filler (BSSF) paste. The BSSF paste was formed by mixing powder with the nominal composition, as listed in Table 1 (Ref. 33), with Vitta-Braz Binder Gel-Grade ST in a ratio of 10 wt-% gel and 90 wt-% powder. For comparison, Table 1 also lists the nominal composition of the Alloy 600 base material (Ref. 32). No means of joint clearance control was employed, as the rods were permitted to move freely in their axial direction by virtue of a 0.005-in.-radius difference with respect to the holes in the fixture plates. Brazing was performed in a high-vacuum furnace with a mechanically backed diffusion pump operating at a pressure no greater than 10^{-5} torr.
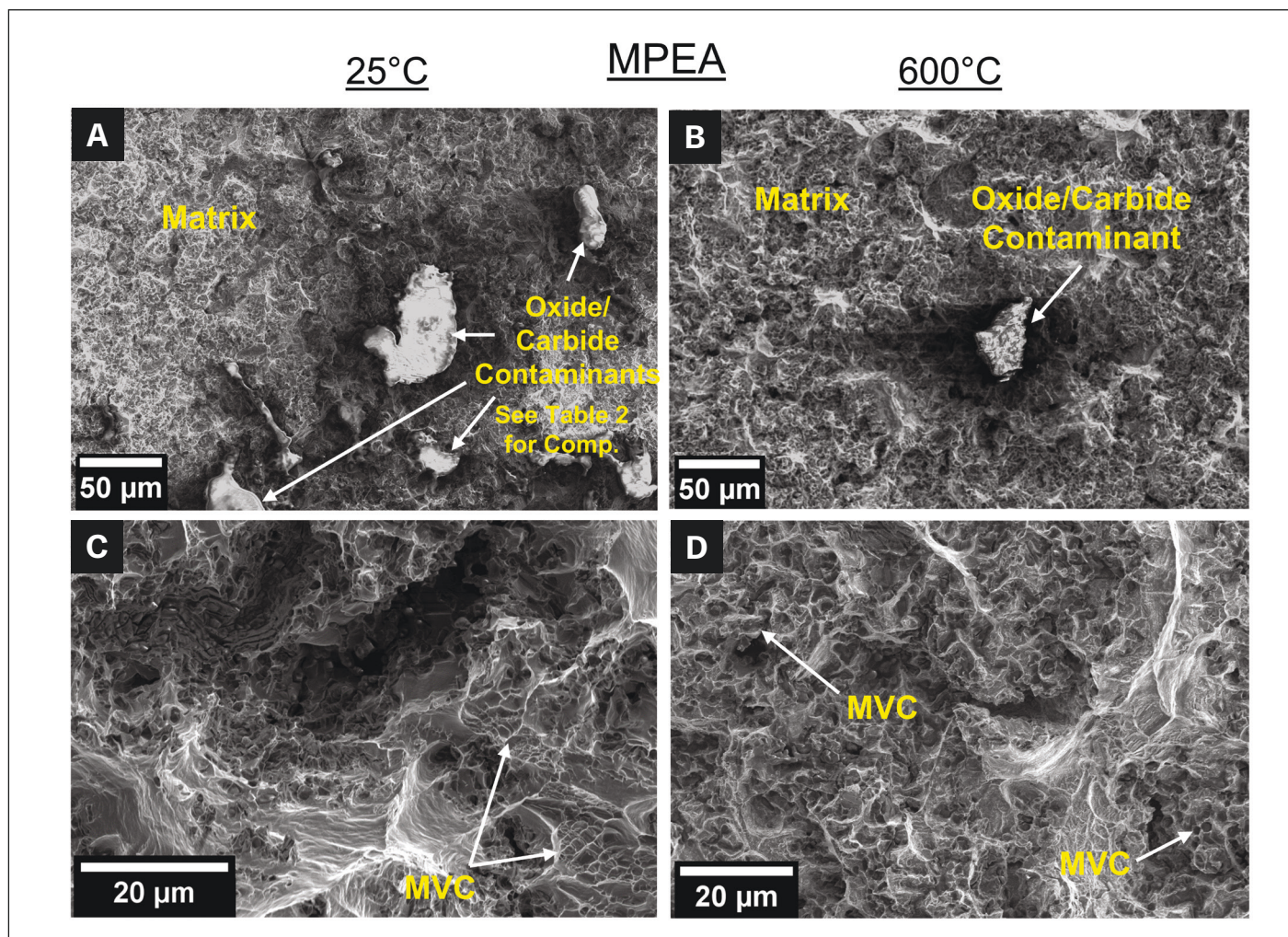
Fig. 6 — SEM micrographs of fracture surfaces following mechanical testing of the MPEA braze: A, B — Low-magnification images highlighting the presence of dispersed contaminant particles on the fracture surfaces. C, D — higher-magnification images displaying ductile MVC. A, C — room temperature tests; B, D — 600°C tests.

Because the MPEA has a reported melting range of 1080–1150°C (Ref. 17), and the melting range of the BSSF filler metal is 971–999°C (Ref. 33), both are viable for brazing Alloy 600 (melting range 1354–1413°C) (Ref. 32). The optimum brazing temperature of 1200°C reported for the MPEA (Ref. 17) was selected for both filler metals to make a direct comparison. The MPEA joints were heated to 1200°C at a rate of 15°C/min and held for 90 min followed by a furnace cool in accordance with the reported optimal thermal profile (Ref. 17, Fig. 3C). To highlight the differences in filler metal performance under similar processing requirements, the BSSF metal brazing procedure outlined in Hawk's work (Ref. 34) was selected because it closely mirrors the overall process time necessary for the MPEA brazing process. The thermal cycle for the BSSF metal joints (Fig. 3D) involved intermediate holding stages during heating at 200°C to remove excess moisture in the paste (at 583°C for binder decomposition and at 900°C for temperature equilibration). The heating rate was 15°C/min between each hold. The final brazing temperature was 1200°C, with a 10-min hold time followed by a furnace cool.

Specimens were either prepared for metallographic examination by diametrically cross sectioning the joint and polishing to a final step of 0.05 μm or machined into ASTM E8M round tensile specimens with a 6-mm gauge diameter and a surface finish of 32 μin — Fig. 3B. Analysis of the microstructure and elemental distribution in the cross section of the joints was performed with a JEOL 7000F field-emission scanning electron microscope (SEM) with an energy dispersive spectrometer (EDS) operating at 20 kV and a 10-mm working distance.

Room temperature and 600°C elevated temperature tensile tests were performed at a strain rate of 1×10^{-3} s^{-1} on an MTS Landmark 22.5 kip load frame equipped with a pyrometer-controlled induction furnace, water-cooled grips, and an elevated-temperature extensometer. Three tensile tests were performed for each condition. For the room temperature tests, digital image correlation (DIC) was used to generate strain-partitioning maps. Prior to testing at 600°C, the pyrometer emissivity was calibrated against a K-type thermocouple contacting base material at the same surface finish as the tensile specimens. Specimens were
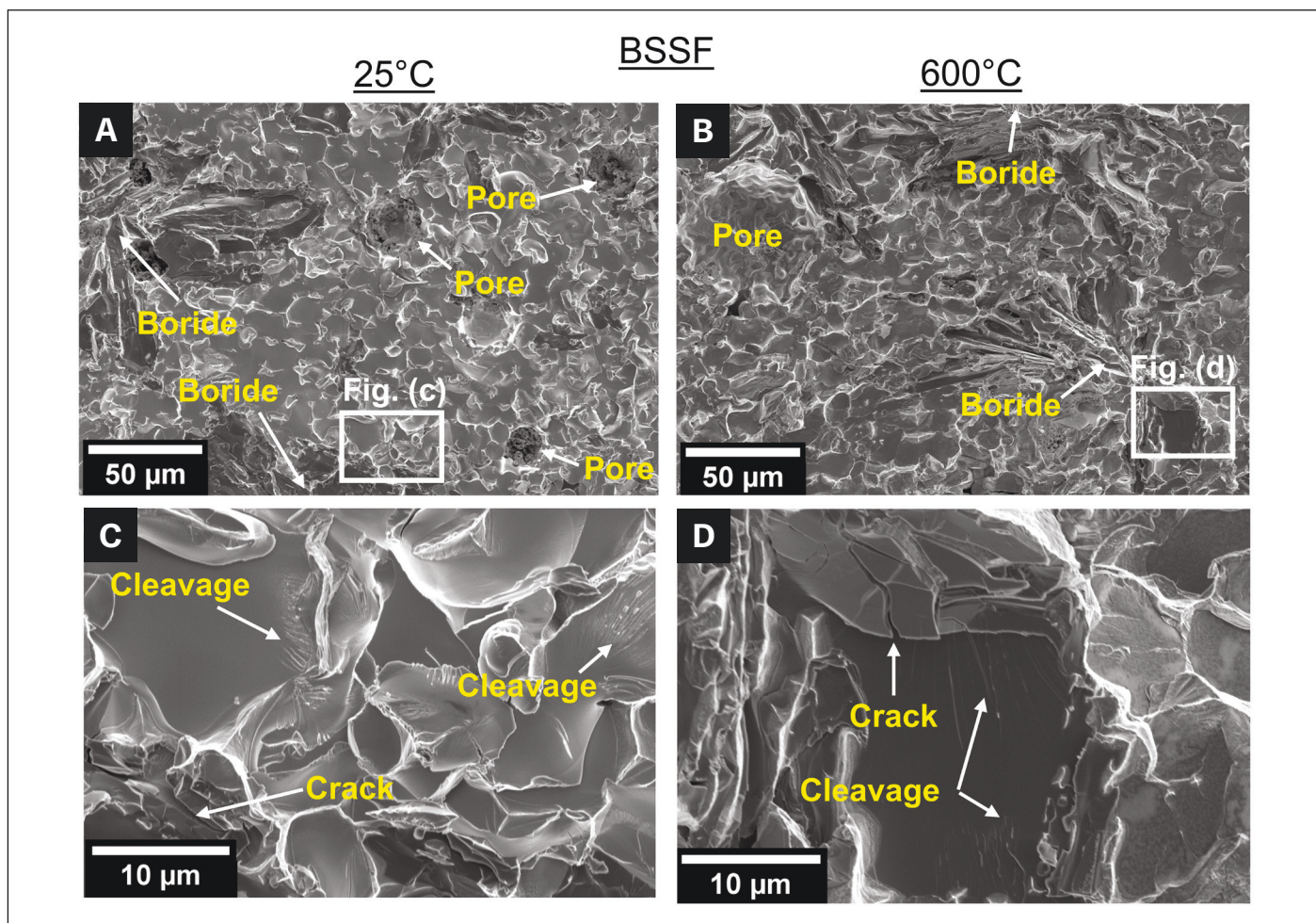
Fig. 7 — SEM micrographs of fracture surfaces following mechanical testing of the BSSF braze: A, B — Low-magnification images displaying boride phase clusters and pore remnants; C, D — higher-magnification images indicating cracking through boride particles and brittle cleavage fracture. A, C — room temperature tests; B, D — 600°C tests.

held at 600°C for 3 min prior to initiating the tensile test. After testing, fracture surfaces were examined using an FEI Helios Nanolab 600i SEM.

Results and Discussion

Braze Microstructure and Composition

Figure 4A and B illustrate macroscopic views of the MPEA and BSSF metal braze joints captured from optical microscopy. Secondary electron images and corresponding EDS element maps of representative areas of joint cross sections are provided in Fig. 4C–F. Large circular pores in the BSSF metal joint can be observed in Fig. 4B. The pores in the MPEA joint were considerably smaller and only observable in the SEM micrograph, as shown in Fig. 4C.

As shown in Fig. 4E and F, a Cr-rich boride phase was observed in eutectic constituents that populated the centerline of the BSSF metal joint. Boron was excluded from the EDS element map in Fig. 4F due to the low signal-to-noise ratio when detecting elements

below carbon in atomic number using EDS. However, the estimated composition of the boride, determined using point-based EDS measurement with a higher signal-to-noise ratio, is provided in Table 2. The extent of the boride phase, limited to within approximately 20 µm of the joint centerline, indicated that isothermal solidification likely occurred during the 10-min holding cycle. However, isothermal solidification was incomplete, and the residual liquid solidified as a eutectic mixture at the joint centerline, as discussed in Fig. 1A. As indicated in Fig. 4C–D, the MPEA braze exhibited no harmful second-phase formation in the solidification microstructure, although Mn and Cu segregation were observed at the centerline of the joint, as detailed in Refs. 17 and 18.

Chromium-rich oxide was observed to discontinuously populate grain boundaries, as shown in Fig. 4D. Of the constituent metallic elements, Cr and Mn have the greatest affinity for oxygen (Ref. 35), which could explain why Cr preferentially oxidizes. The estimated composition of this oxide from point-based EDS is provided in Table 2. While the point-based data indicated more Ni than Cr in the assessed region, the particles were small enough that the EDS interaction volume likely encompassed both the particle and

Table 2 — Compositions (at.-%) of Nonsolid-Solution Particles Appearing in the MPEA or BSSF Metal Braze*

Element (at.-%)	B	C	O	Mg	Al	Si	Ca	Ti	Cr	Mn	Fe	Co	Ni	Cu
Cr-rich oxide particles at grain boundaries in the MPEA filler metal braze	—	9.1	56.6	—	—	—	—	—	5.1	4.8	3.0	2.6	17.5	1.2
Cr-rich boride particles in the BSSF metal cross section	69.3	—	—	—	—	—	—	—	28.9	0.6	—	—	1.2	—
Contaminant particles on the MPEA fracture surface	—	33.5	35.0	2.5	1.3	3.2	3.4	6.6	—	0.1	0.03	—	0.2	—

*Note: Compositions represent an average of point-based EDS analyses taken over five distinct particles.

some of the surrounding matrix. Local Cr and oxygen enrichment in the particle is conclusively demonstrated in the EDS map insets provided in Fig. 4D.

Mechanical Performance

Figure 5 summarizes the mechanical testing results for joints brazed with the MPEA and BSSF filler metals. Figure 5A and B provide the individual engineering stress-strain curves for each specimen tested. The contour maps in the insets, along with Fig. 5C, directly compare strain partitioning behavior measured through room-temperature DIC. Figure 5D summarizes the statistical distribution of the mechanical properties for the two joints under both testing conditions. As indicated, the average total elongation for the MPEA braze was 15.2 and 9.9% for room-temperature and 600°C testing, respectively, while elongation was limited to less than 1% for the BSSF braze under both testing conditions. The DIC strain data demonstrated that the MPEA-brazed specimens underwent extensive yielding throughout the gauge length of the specimen, achieving a uniform elongation of approximately 8%, as shown by the legend in the inset of Fig. 5A. In contrast, the BSSF braze only yielded in highly localized deformation within the joint — Fig. 5B. Both specimens ultimately experienced interfacial failure.

Figures 6 and 7 provide a fractographic assessment of the mechanical behavior of the MPEA filler and BSSF braze metals, respectively. As illustrated in Fig. 6A and B, dispersed contaminant inclusions with an irregular morphology up to 50 μm in size were observed on the MPEA braze fracture surface. The average composition of five of these particles is provided in Table 2. The composition indicated that the particles were mixed carbides and oxides of several contaminant elements, including Mg, Si, Al, Ca, and Ti, with low concentrations of any of the MPEA or Alloy 600 primary constituents. The presence of these contaminant

elements indicated room for improvement in avoiding contamination of the manufacturing process described in Gao et al. (Ref. 17). Despite the contamination particles, the fracture surfaces of the MPEA braze were dominated by extensive regions of ductile microvoid coalescence (MVC) — Fig. 6C, D. In contrast, no MVC was identified in the BSSF fractographs displayed in Fig. 7A and B. Two features on these fracture surfaces can be correlated with the cross-sectional micrographs displayed in Fig. 4. Circular features ranging from 20 to 50 μm in diameter (Fig. 7A) were identified as the remnants of preexisting pores at the braze interface visible in Fig. 4B. Clusters of second phase that possessed a flower-like morphology, shown in Fig 7A andB, were identified as the Cr-rich boride seen in Fig. 4E and F. The identity of these second phases was confirmed through EDS analysis on the fracture surfaces.

Figure 7C and D shows the BSSF metal fracture surfaces at higher magnification. Cracks were clearly observed adjacent to flat, planar features that possessed branching "river" markings around the borides. This set of features is consistent with crack nucleation and brittle cleavage fracture at the interface between a boride particle and matrix. Cracks were not observed to nucleate from the pore remnants shown in Fig. 7A and B. Therefore, the microstructural feature dominating the failure mechanism of the BSSF metal braze was the Cr-rich boride phase, despite the porosity observed in Fig. 4B.

The BSSF metal brazing process employed in this work can be considered sufficiently representative of the brazes that fail by the same mechanism commonly reported in literature (Refs. 7, 8), although the amount of athermally solidified eutectics in this work may be more than the optimal or desirable level. It is acknowledged that substantially longer braze hold times would likely reduce the extent of the eutectic microconstituent containing the boride phase by promoting additional isothermal solidification. However, as detailed previously, it is difficult to completely eliminate boride phases, as evidenced by the reten-

tion of diffusion-induced borides in the microstructure of a TLP bond, even after complete isothermal solidification was achieved (Ref. 3). It is also notable that the elongation of the MPEA braze reported in Fig. 5 was greater than almost all reported values for brazes employing conventional filler metals (Ref. 1).

No crack inititation sites could be easily identified via fractography on the MPEA braze fracture surface due to the extensive ductile MVC. The elongation data in Fig. 5D (green bars) and the individual stress-strain curves in Fig. 5A and B indicate that the ductility of the MPEA braze, while always superior to that of the BSSF metal, exhibited considerable variation for both room-temperature and elevated-temperature tests. The inconsistent elongation demonstrated by the MPEA braze suggests inconsistency in the nature of stress concentrators and fracture nucleation sites contained within the braze. The irregular morphology of the porosity visible in the cross section (Fig. 4C), along with the broad distribution in size, suggest that this porosity may cause variable stress concentration and contribute to the scatter in the ductility.

Alternatively, the presence of Cr-rich oxides along grain boundaries (Fig. 4D) and the larger, dispersed oxide and carbide inclusions on the fracture surfaces of the MPEA braze (Fig. 6A, B) could play a role in nucleating fracture and ultimate failure. If the large inclusions govern failure, it is likely that further improvement in performance could be achieved by developing a cleaner means of filler metal production. The current production method by arc casting and cold rolling (Ref. 17) is not yet optimized to mitigate contaminants and oxidation, as emphasized by the presence of several contaminant elements (Table 2) in the fracture-surface particles. Regardless of which feature is primarily involved, the ductility data demonstrated that the MPEA filler metal possessed substantial tolerance to defects in the braze microstructure before failure was initiated.

The average yield strengths (red bars in Fig. 5D) exhibited by the two braze specimens were comparable to within one standard deviation at both room temperature and 600°C, as indicated by the error bars. The ultimate tensile strength (blue bars in Fig. 5D) was greater for the MPEA than the BSSF metal, due to the significant work hardening experienced during plastic deformation (Fig. 5A). Thus, it was concluded that the MPEA braze offers superior ductility over the BSSF braze and comparable strength at both room temperature and 600°C, which together represent a marked improvement in the fracture toughness.

The room-temperature yield strengths measured were 218 MPa for the MPEA braze and 230 MPa for the BSSF braze. These values were 33.4 and 35.2% of the measured value of 653 MPa for the Alloy 600 base material tested in the as-received condition. However, metallographic assessment performed on as-received Alloy 600 and material that was subjected to the MPEA brazing thermal cycle indicated that the majority of this reduction in yield strength could be attributed to grain growth in the base material. The grain size in the as-received condition was found to be 9 µm ±1 µm, and the grain size in the material that underwent the thermal cycle was found to be 301 µm ± 83 µm. These data were analyzed in conjunction with a reported Hall-Petch-type relationship for Alloy 600 (Ref. 36), and it was found that this grain growth alone could account for 84% of the observed yield strength debit in the brazes. Considering the empirical nature of the Hall-Petch relationship and the DIC data that indicated uniform initial yielding throughout the specimen gauge length, it is reasonable to propose that observed yield strength reduction is fully accounted for by grain growth in the base material. This suggests there is no inherent weakness in the MPEA filler metal, and higher joint yield strengths could be achieved when using alternative brazing methods that limit the heat input into base materials or brazing other Ni-based superalloy materials that are more resistant to grain growth.

Hence, applying this MPEA filler metal or further fine-tuned compositions to braze precipitation-strengthened superalloys is an area of promising future research. Additionally, the high-temperature testing matrix should be expanded in future studies to include higher operating temperatures (e.g., 800°C) that mimic the harsh operating conditions of the superalloy substrate. Creep and fatigue testing should also be performed in future studies to evaluate the endurance of the MPEA filler metal's beneficial mechanical properties in a working environment.

Conclusions

In summary, this study confirms that the metallurgical benefits of the new MPEA filler metal, as originally reported in Gao et al. (Ref. 17), extend to tensile deformation at both room temperature and elevated temperature. The single-phase solidification behavior of the filler metal and the absence of brittle phases introduced by conventional MPD elements offer vastly improved ductility over B- and Si-suppressed fillers metals and comparable strength. The extent of isothermal solidification is unimportant for the MPEA filler metal offering ductile performance after relatively short process durations. Fractography on the specimens indicated that boride phases, not pores, were the primary factor limiting the ductility of the BSSF brazes. The superior tensile ductility exhibited by the MPEA braze is due to a single-phase FCC microstructure and fracture dominated by MVC. The ductility could be further improved by a cleaner filler metal production process with less oxides and better controlled porosity in the MPEA braze. While joints brazed with both filler metals exhibited yield strengths that were only fractions of that of the as-received base material, this discrepancy could be nearly wholly accounted for by grain growth in the base material during the brazing thermal cycle.

References

1. Huang, X., and Miglietti, W. 2012. Wide gap braze repair of gas turbine blades and vanes — A review. *Journal of Engineering for Gas Turbines and Power* 134(1). DOI: 10.1115/1.4003962

2. Tung, S. K., Lim, L. C., and Lai, M. O. 1995. Microstructural evolution and control in BNi-4 brazed joints of nickel 270. *Scripta Materialia* 33(8): 1253–1259. DOI: 10.1016/0956-716X(95)00352-V

3. Pouranvari, M., Ekrami, A., and Kokabi, A. H. 2008. Microstructure development during transient liquid phase bonding of GTD-111 nickel-based superalloy. *Journal of Alloys and Compounds* 461(1–2): 641–647. DOI: 10.1016/j.jallcom.2007.07.108

4. Pouranvari, M., Ekrami, A., and Kokabi, A. H. 2009. Effect of bonding temperature on microstructure development during TLP bonding of a nickel base superalloy. *Journal of Alloys and Compounds* 469(1–2): 270–275. DOI: 10.1016/j.jallcom.2008.01.101

5. Gale, W. F., and Wallach, E. R. 1991. Microstructural development in transient liquid phase bonding. *Metallurgical Transactions A* 22: 2451–2457. DOI: 10.1007/BF02665011

6. Gale, W. F., and Butts, D. A. 2004. Transient liquid phase bonding. *Science and Technology of Welding and Joining* 9(4): 283–300. DOI: 10.1179/136217104225021724

7. He, Q., Zhu, D., Dong, D., Xu, M., Wang, A., and Sun, Q. 2019. Effect of bonding temperature on microstructure and mechanical properties during TLP bonding of GH4169 superalloy. *Applied Sciences* 9(6): 1112. DOI: 10.3390/app9061112

8. Jamaloei, A. D., Khorram, A., and Jafari, A. 2017. Characterization of microstructure and mechanical properties of dissimilar TLP bonding between IN718/IN600 with BNi-2 interlayer. *Journal of Manufacturing Processes* 29: 447–457. DOI: 10.1016/j.jmapro.2017.09.010

9. Yang, Y. H., Xie, Y. J., Wang, M. S., and Ye, W. 2013. Microstructure and tensile properties of nickel-based superalloy K417G bonded using transient liquid-phase infiltration. *Materials and Design* 51: 141–147. DOI: 10.1016/j.matdes.2013.04.024

10. Kim, Y. H., Kim, K. T., and Kim, I. H. 2006. Effect of mixing ratio on mechanical properties of wide-gap brazed Ni-based superalloy with Ni-Si-B alloy powder. *Key Engineering Materials* 306–308: 935–940. DOI: 10.4028/www.scientific.net/KEM.306-308.935

11. Kim, Y. H., Kim, I. H., and Kim, C. S. 2005. Effect of process variables on microstructure and mechanical properties of wide-gap brazed IN738 superalloy. *Key Engineering Materials* 297–300: 2876–2882. DOI: 10.4028/www.scientific.net/KEM.297-300.2876

12. Kim, Y. H., and Kwun, S. I. 2006. Microstructure and mechanical properties of the wide-gap region brazed with various powder mixing ratios of additive to filler metal powders. *Solid State Phenomena* 118: 479–484. DOI: 10.4028/www.scientific.net/SSP.118.479

13. Schwartz, M. M. 1975. Applications for gold-base brazing alloys. *Gold Bulletin* 8(4): 102–110.

14. Khorram, A., Ghoreishi, M., Torkamany, M. J., and Bali, M. M. 2014. Laser brazing of Inconel 718 alloy with a silver based filler metal. *Optics & Laser Technology* 56: 443–450. DOI: 10.1016/j.optlastec.2013.08.022

15. Miglietti, W., and Du Toit, M. 2010. High strength, ductile braze repairs for stationary gas turbine components — Part I. *Journal of Engineering for Gas Turbines and Power* 132(8): 082102-1–082102-12. DOI: 10.1115/GT2008-51133

16. Miglietti, W., and Du Toit, M. 2010. High strength, ductile braze repairs for stationary gas turbine components — Part II. *Journal of Engineering for Gas Turbines and Power* 132(8): 082103-1–082103-10. DOI: 10.1115/1.4000149

17. Gao, M., Schneiderman, B., Gilbert, S. M., and Yu, Z. 2019. Microstructural evolution and mechanical properties of nickel-base superalloy brazed joints using a MPCA filler. *Metallurgical and Materials Transactions A* 50: 5117–5127. DOI: 1007/s11661-019-05386-8

18. Schneiderman, B., Chuang, A. C., Kenesei, P., and Yu, Z. 2021. In-situ synchrotron diffraction and modeling of non-equilibrium solidification of a MnFeCoNiCu alloy. *Scientific Reports* 11(1): 5921. DOI: 10.1038/s41598-021-85430-z

19. Cantor, B., Chang, I. T. H., Knight, P., and Vincent, A. J. B. 2004. Microstructural development in equiatomic multicomponent alloys. *Materials Science and Engineering A* 375–377: 213–218. DOI: 10.1016/j.msea.2003.10.257

20. Yeh, J. W., Chen, S. K., Lin, S. J., Gan, J. Y., Chin, T. S., Shun, T. T., Tsau, C. H., and Chang S. Y. 2004. Nanostructured high-entropy alloys with multiple principal elements: Novel alloy design concepts and outcomes. *Advanced Engineering Materials* 6(5): 299–303. DOI: 10.1002/adem.200300567

21. Yeh, J. W. 2013. Alloy design strategies and future trends in high-entropy alloys. *JOM* 65(12): 1759–1771. DOI: 10.1007/s11837-013-0761-6

22. Yeh, J. W., Chang, S. Y., Hong, Y. D., Chen, S. K., and Lin, S. J. 2007. Anomalous decrease in x-ray diffraction intensities of Cu–Ni–Al–Co–Cr–Fe–Si alloy systems with multi-principal elements. *Materials Chemistry and Physics* 103(1): 41–46. DOI: 10.1016/j.matchemphys.2007.01.003

23. Tsai, K. Y., Tsai, M. H., and Yeh, J. W. 2013. Sluggish diffusion in Co-Cr-Fe-Mn-Ni high-entropy alloys. *Acta Materialia* 61(13): 4887–4897. DOI: 10.1016/j.actamat.2013.04.058

24. Jin, K., Zhang, C., Zhang, F., and Bei, H. 2018. Influence of compositional complexity on interdiffusion in Ni-containing concentrated solid solution alloys. *Materials Research Letters* 6(5): 293–299. DOI: 10.1080/21663831.2018.1446466

25. Otto, F., Yang, Y., Bei, H., and George, E. P. 2013. Relative effects of enthalpy and entropy on the phase stability of equiatomic high-entropy alloys. *Acta Materialia* 61(7): 2628–2638. DOI: 10.1016/j.actamat.2013.01.042

26. Miracle, D. B., and Senkov, O. N. 2017. A critical review of high entropy alloys and related concepts. *Acta Materialia* 122: 448–511. DOI: 10.1016/j.actamat.2016.08.081

27. Hume-Rothery, W. 1969. *Atomic Theory for Students of Metallurgy*. London, UK: The Institute of Metals.

28. Hume-Rothery, W., and Powell, H. M. 1935. On the theory of super-lattice structures in alloys. *Crystalline Materials* 91(1–6): DOI: 10.1524/zkri.1935.91.1.23

29. Hume-Rothery, W., Smallman, R. E., and Haworth, C. W. 1969. *The Structure of Metals and Alloys*. London, UK: The Institute of Metals.

30. Zhang, Y., Zhou, Y. J., Lin, J. P., Chen, G. L., and Liaw, P. K. 2008. Solid-solution phase formation rules for multi-component alloys. *Advanced Engineering Materials* 10(6): 534–538. DOI: 10.1002/adem.200700240

31. Guo, S., Ng, C., Lu, J., and Liu, C. T. 2011. Effect of valence electron concentration on stability of fcc or bcc phase in high entropy alloys. *Journal of Applied Physics* 109(10): 103505. DOI: 10.1063/1.3587228

32. Inconel Alloy 600. 2008. Special Metals Corp.

33. AMS 4777 (BNi2) Technical Data. Prince and Izant Co.

34. Hawk, C. 2016. Wide gap braze repairs of nickel superalloy gas turbine components. George S. Ansell Department of Metallurgical and Materials Engineering, Colorado School of Mines, Golden, Colo.

35. Khanna, A. S. 2018. High-temperature oxidation. *Handbook of Environmental Degradation of Materials*, 3rd edition. Ed. Kutz, M. Norwich, N.Y.: William Andrew Publishing, pp. 117–132. DOI: 10.1016/B978-0-323-52472-8.00006-X

36. Song, K. H., Fujii, H., and Nakata, K. 2009. Effect of welding speed on microstructural and mechanical properties of friction stir welded Inconel 600. *Materials and Design* 30(10): 3972–3978. DOI: 10.1016/j.matdes.2009.05.033

BENJAMIN SCHNEIDERMAN, **OLIVIA DeNONNO**, **JONAH KLEMM-TOOLE,** and **ZHENZHEN YU** (*zyu@mines.edu*) are with the George S. Ansell Department of Metallurgical and Materials Engineering, Colorado School of Mines, Golden, Colo.